General Two-Phase Routes to Synthesize Colloidal Metal Oxide Nanocrystals: Simple Synthesis and Ordered Self-Assembly Structures

Thanh-Dinh Nguyen and Trong-On Do*

Department of Chemical Engineering, Laval University, Quebec G1K 7P4, Canada

Received: January 9, 2009; Revised Manuscript Received: May 1, 2009

Different two-phase approaches have been developed for the synthesis of two classes of monodisperse colloidal metal oxide nanocrystals (NCs): rare earth oxide NCs and transition metal oxide NCs. These routes were simple and inexpensive, using metal salts instead of organometallic compounds, with mild reaction conditions, easily controlled size and shape, and multigram-scale products. The obtained products were characterized by transmission electron microscopy (TEM), selected area electron diffraction (SAED), X-ray diffraction (XRD), X-ray photoelectron spectra (XPS), Fourier transform infrared absorption spectroscopy (FTIR), and nitrogen adsorption−desorption isotherms (BET). The possible mechanisms for the formation and growth of nanocrystals were discussed. Accordingly, *tert*-butylamine (nucleophile agent) and ethanol (reduced agent) are the key factors for the formation of rare earth oxide NCs and transition metal oxide NCs, respectively. Different sizes and shapes of monodisperse nanoparticles such as spherical, cubic, peanut, rod, and hexagonal NCs were obtained, depending on the nature of metal precursors. Furthermore, the effect of monomeric precursor concentration, type of precursors, and reaction time on the size and shape of the products was also studied. The SAED patterns of the obtained NC samples show a set of sharp spots that are characteristic of single crystalline structures indexed accordingly with the structures determined by the XRD spectra. The XPS results revealed the presence of two oxidation states of cerium, samarium, manganese, and cobalt on the nanocrystal surface, whereas it seems only one oxidation state is present on the surface for Y, Cr, La, Gd, and Er oxide nanocrystals. A large O 1s XPS peak attributed to two oxygen components for these Ce, Sm, Mn, and Co oxide NC samples refer to the defected structure. Our approaches may be also applicable to synthesize other uniform metal oxide NCs as well as doped metal oxide NCs and multicomponent NCs.

1. Introduction

Colloidal inorganic nanocrystals (NCs), 1−100 nm in size, are versatile building blocks for constructing diverse superstructures, functional mesocrystals, and new nanodevices, which can expect to find useful applications in catalysis, magnetic data storage, solar cells, lithium ion batteries, medicine, etc.[1−4] Assembling the single nanocrystals into ordered lattice structures that is "bottom up assembly" is an attractive way for us to design systems possessing the novel physicochemical properties that differ drastically from their bulk counterparts.[5,6] Thus, the development and innovation of new synthetic strategies for high-quality oxide nanocrystals have been among the key issues in scientific research.[7]

Numerous methods have been well-documented in several recent review articles for the synthesis of a broad range of nanocrystals, including the hydrolytic and nonhydrolytic sol−gel process,[8] solvo−hydrothermal treatment,[9] and thermal decomposition.[10] Size and shape controls for nanocrystals can be obtained via single-phase or two-phase methods. The single-phase method is always used for the synthesis of colloidal oxide nanocrystals.[11,12] Furthermore, the two-phase synthetic method was first reported by Brust et al.[13] for the synthesis of gold nanoparticles and other noble metal nanoparticles such as Ag, Pt, and Au.[14] Related progress using the two phase approach was also extended to the synthesis of metal oxide and semiconductor nanocrystals.[15] Compared to the single-phase approach, the two-phase strategy can obtain the products with good crystallinity under relatively mild adopted conditions because the presence of the water phase in bulk solution generally increases the speed of the growth process, which was previously reported by Lu et al.[16] and recently by our group.[17] Particle size and shape can also be controlled because of the relatively slow nucleation process, which was demonstrated by An et al.[18] Many attempts have been made to use the design and synthesis of a variety of NCs and this two-phase approach to explore their properties and potential applications. For example, Pan et al.[19,20] reported a hydrothermal two-phase route to synthesize monodisperse TiO_2 and ZrO_2 NCs from the hydrolysis of titanium(IV) isopropoxide and zirconium(IV) isopropoxide, respectively, in a water−toluene mixture. Kaskel et al.[21] reported the synthesis of $BaTiO_3$ nanocrystals using mixed titanium(IV)-*n*-butoxide and barium acetate precursors. Furthermore, Adschiri et al.[22] modified this reaction system for the synthesis of CeO_2 nanocubes using cerium hydroxide precursors under supercritical water conditions. The product shape could be controlled by tuning the interaction of organic molecules with various crystallographic planes of fluorite cubic ceria. More recently, our group[23] developed a modified two-phase method for the synthesis of alkyl chain-capped metal particles (e.g., Cu and Au) and metal oxide nanoparticles (CeO_2, TiO_2, and ZrO_2), followed by their cooperative assemblage into unusual hybrid metal/metal oxide NCs mesostructured materials. Indeed, these metal/metal oxide hybrid materials exhibited high surface areas, narrow pore size distributions, and exceptional catalytic properties in the oxidation of CO, even surpassing the

* To whom correspondence should be addressed. E-mail: Trong-On.Do@gch.ulaval.ca.

10.1021/jp900226m CCC: $40.75
Published on Web 06/05/2009

performance of commercial noble metal catalysts. In addition, the controlled size and shape of vanadia and samaria NCs were also developed using inexpensive metal precursors and multigram scales in a single run.[17,24] Even though the two-phase methods have been shown to synthesize various metal oxide nanocrystals, the development of general and simple two-phase methods for the synthesis of a variety of NCs with a desired shape and size control using inexpensive precursors still faces challenges.

In this paper, we report two different general two-phase approaches for the synthesis of two classes of colloidal metal oxide nanocrystals (NCs). These are the rare earth oxide NCs and transition metal oxide NCs, with controlled size and shape, through the hydrolysis of corresponding inorganic salts or metal−surfactant complexes in the water−toluene system. These synthetic approaches have several advantages, including relatively mild conditions, easy manipulation, and large-scale products. The possible mechanisms for the formation of alkyl-capped oxide nanocrystals in each route are also proposed. Furthermore, the effect of various synthetic reaction parameters, including precursor concentration, type of precursors, and reaction time on the shape evolution of nanocrystalline oxides are also studied.

2. Experimental Section

2.1. Starting Materials. All chemicals were used as received without further purification. Cerium(III) nitrate hexahydrate ($Ce(NO_3)_3 \cdot 6H_2O$, 99.9%), cerium(III) acetate hydrate [$Ce(ac)_3 \cdot xH_2O$, 99.9%], samarium(III) nitrate hexahydrate [$Sm(NO_3)_3 \cdot 6H_2O$, 99.9%], yttrium(III) nitrate hexahydrate [$Y(NO_3)_3 \cdot 6H_2O$, 99.9%], lanthanium (III) nitrate hexahydrate [$La(NO_3)_3 \cdot 6H_2O$, 99.9%], gadolinium(III) nitrate hexahydrate [$Gd(NO_3)_3 \cdot 6H_2O$, 99.9%], erbium(III) nitrate hydrate [$Er(NO_3)_3 \cdot xH_2O$, 99.9%], manganese(III) nitrate tetrahydrate [$Mn(NO_3)_2 \cdot 4H_2O$, 99%], chromium(III) chloride hexahydrate ($CrCl_3 \cdot 6H_2O$, 99%), cobalt(II) nitrate hexahydrate [$Co(NO_3)_3 \cdot 6H_2O$, 98%], nickel(II) nitrate hexahydrate [$Ni(NO_3)_2 \cdot 6H_2O$, 99.999%], oleic acid ($C_{18}H_{35}COOH$ or OA, technical grade, 90%), oleylamine ($C_{18}H_{35}NH_2$ or OM, technical grade, 70%), potassium oleate ($C_{18}H_{35}COOK$, 40% water), and *tert*-butylamine [$(CH_3)_3CNH_2$, 98%] were purchased from Sigma-Aldrich. All solvents used such as toluene and absolute ethanol were of analytical grade and purchased from Reagent ACS.

2.2. Nanocrystal Synthesis. All NCs in this work were synthesized in a two-phase system and stabilized with hydrophobic molecules containing long alkyl chains (C_{18}). Detailed information on the synthesis of metal oxide NCs is given below.

2.2.1. Synthesis of Rare Earth Oxide Nanocrystals. *2.2.1.1. Synthesis of Rare Earth Oxide Nanocrystals (e.g., Sm_2O_3 and CeO_2 NCs) Using Rare Earth Salt Precursors.* The synthetic procedures were similar to that of Sm_2O_3 NCs, which was recently reported by our group.[24] Typically, 20 mL of an aqueous solution (0.015−0.120 mol/L) containing a metal salt [0.3−2.4 mmol, $Sm(NO_3)_3 \cdot 6H_2O$, $Ce(NO_3)_3 \cdot 6H_2O$, or $Ce(ac)_3$], and *tert*-butylamine (0.15 mL) was mixed with an organic solution of oleic acid (1.5 mL) and toluene (20 mL). The resulting mixture was transferred to a 60 mL Teflon-lined stainless steel autoclave in the ambient environment without stirring. The sealed autoclave was heated at 180 °C for 24 h. Afterward, the system was cooled to room temperature by submerging the reactor in a water bath. The nanocrystal solution was precipitated with the excess volume of ethanol. The purified products were separated by centrifugation and easily redispersed in a nonpolar solvent (e.g., toluene, hexane, and chloroform). The precipitation−redispersion process was repeated several times to purify the producing nanocrystals.

2.2.1.2. Synthesis of Rare Earth Oxide Nanocrystals Using Rare Earth−Surfactant Complex Precursors (e.g., RE = Er, Gd, La, or Y). The synthesis of rare earth (RE) oxide nanocrystals consists of two steps: (i) preparation of rare earth complex precursors from rare earth salts and (ii) the formation of NCs.

(i) To prepare rare earth−oleate complexes, we produced an organic solution by adding 20 mL of toluene into the ethanol solution (6.4 mL) containing potassium oleate (0.85 g or 1.1 mmol). Subsequently, the organic phase was mixed with 12.8 mL of an aqueous solution of $RE(NO_3)_3 \cdot 6H_2O$ (0.36 mmol, RE = Er, Gd, La, or Y) and transferred to a flask. The stock two-phase mixture was heated to 70 °C for 60 min with stirring vigorously, and the organic solution turned light yellow after the reaction, indicating the occurrence of the coordinative reaction between a rare earth cation and oleate anion for the complex formation. The RE^{3+}/$oleate^-$ molar ratio is close to 1:3, $RE(OA)_3$. The upper homogeneous toluene supernatant phase (20 mL) containing RE−oleate complexes was isolated using a separatory funnel. The yields for these rare earth complexes were between 85% and 95%.

(ii) To form Er_2O_3, Gd_2O_3, La_2O_3, and Y_2O_3 nanocrystals, we typically added 5 mL of oleylamine to the above-prepared rare earth complex solution (20 mL, 0.018 mol/L) under stirring for 10 min. Then, the organic solution was transferred to a 60 mL Teflon-lined stainless steel autoclave containing an aqueous solution (20 mL) of *tert*-butylamine (0.15 mL). The autoclave was seated and heated to the crystallization temperature at 180 °C for 24 h.

2.2.2. Synthesis of Transition Metal Oxide Nanocrystals (TMO-NCs) (e.g., Mn_3O_4, Cr_2O_3, Co_3O_4, or NiO NCs Using Transition Metal Salts as Precursors. Typically, a homogeneous ethanol solution (10 mL) containing potassium oleate (3 g) was added to the organic solution of toluene (20 mL) and oleic acid (2 mL) and then was mixed with 20 mL of an aqueous solution (0.08 M, 1.6 mmol) containing a metal salt, including $Mn(NO_3)_3$, $CrCl_3$, $Co(NO_3)_2$, and $Ni(NO_3)_2$, for the formation of a two-phase reactive mixture, in which the oleate anions disperse into the organic phase, while the ethanol and potassium (K^+) cations enter into the aqueous phase. The two-phase mixture was transferred to a Teflon-lined stainless steel autoclave and heated to 180 °C for 24 h. The yield of the products was more than 85%.

2.3. Characterization. The particle sizes and shapes of the synthesized oxide nanocrystals were determined at 120 kV by a JEOL JEM 1230 transmission electron microscope (TEM). Samples were prepared by placing a drop of a dilute toluene dispersion of nanocrystals onto a 200 mesh carbon-coated copper grid and immediately evaporated at ambient temperature. The average particle dimensions were determined by size distribution diagrams, which were obtained from about 100−150 particles in representative TEM pictures of each sample.

The nanocrystal products were characterized on a Bruker SMART APEX II X-ray diffractometer and operated at 1200 W power (40 kV, 30 mA) to generate Cu Kα radiation (λ = 1.5418 Å). The X-ray photoelectron spectra (XPS) were taken on a photoelectron spectrometer (Kratos Axis-Ultra) with a monochromatic X-ray source of Al Kα. The positions of the XPS peaks were corrected using the C 1s peak at 285 eV as a reference. The peaks were deconvoluted by means of a standard CasaXPS software (v.2.3.13; product of CasaXPS Software Ltd., U.S.A.) in order to resolve the separate constituents after

TABLE 1: Synthesis Conditions and Morphologies of the As-Made Capped Metal Oxide Nanocrystals via Hydrothermal Two-Phase Routes

sample[a]	precursor	precursor concn (M)	aqueous phase (mL)	organic phase	surfactant (mL)	time (h)	product	morphology
				rare earth oxide nanocrystals (Schemes 1A,B)				
1	$Sm(NO_3)_3$	0.120	water, TBA[b]	toluene	OA[b]	24	Sm_2O_3	rod
2	$Ce(NO_3)_3$	0.120	water, TBA	toluene	OA	24	CeO_2	cubic, elongated cubic self-assembly
3	$Ce(ac)_3$	0.120	water, TBA	toluene	OA	24	CeO_2	agglomerated cubic self-assembly
4	Er−oleate	0.018	water, TBA	toluene	OM[b]	24	Er_2O_3	spherical self-assembly
5	Gd−oleate	0.018	water, TBA	toluene	OM	24	Gd_2O_3	spherical,peanut
6	La−oleate	0.018	water, TBA	toluene	OM	24	La_2O_3	short rod
7	Y−oleate	0.018	water, TBA	toluene	OM	24	Y_2O_3	long rod
				transition metal oxide nanocrystals (Scheme 2)				
8	$Mn(NO_3)_2$	0.08	water, ethanol	toluene, KOA[b]	OA	24	Mn_3O_4	hexagonal self-assembly
9	$CrCl_3$	0.08	water, ethanol	toluene, KOA	OA	24	Cr_2O_3	dot
10	$Co(NO_3)_2$	0.08	water, ethanol	toluene, KOA	OA	24	Co_3O_4	spherical self-assembly
11	$Co(NO_3)_2$	0.08	water, ethanol	toluene, KOA	OA	18	Co_3O_4	cubic
12	$Co(NO_3)_2$	0.08	water, ethanol	toluene, KOA	OA	12	Co_3O_4	cubic,assembled cubic
13	$Ni(NO_3)_2$	0.08	water, ethanol	toluene, KOA	OA	24	NiO	hexagonal

[a] All samples were synthesized by solvothermal processes at 180 °C. [b] TBA (*tert*-butylamine), KOA (potassium oleate), OA (oleic acid), and OM (oleylamine).

background subtraction. Fourier transform infrared absorption (FTIR) spectra were measured with a FTS 45 infrared spectrophotometer using the KBr pellet technique. The specific area was calculated from the linear part of the Brunauer−Emmett−Teller (BET) equation ($P/P_0 \approx 0.05-0.20$). The pore size distribution was obtained from the analysis of the desorption branch of the isotherms using the Barrett−Joyner−Halenda model.

3. Results and Discussion

All of the syntheses in this study were carried out in a two-phase water−toluene system by mixing metal sources and capping agents. After hydrothermal synthesis, the capped nanocrystal products were highly dispersed in the toluene phase, and no product was observed in the water phase. The NC product in the toluene phase was precipitated by adding excess of ethanol and recovered by centrifugation. Table 1 summarizes the synthesis conditions, the metal precursors, and capping ligands for the synthesis of nanocrystals (NCs) as well as the size and shape of the as-made samples determined by transmission electron microscopy (TEM). Furthermore, even after calcination, no significant change in the morphology of these samples was observed (S-Figure 9 of the Supporting Information). This could be due to the particle surface protected by capping agents during thermal treatment. In this study, we have developed two different simple and general two-phase routes for the synthesis of metal oxide NCs of two-group elements: rare earths, Sm, Ce, Er, Gd, La, and Y (Schemes 1A,B) and transition metals, Mn, Cr, Co, and Ni (Scheme 2), using metal salts as starting precursors. There are some advantageous for these routes because of the use of inorganic salt precursors, instead of expensive metal alkoxides, and quite mild synthetic conditions. Particularly, these synthesis methods are scalable to multigram using the same conditions used in the milligram ones as shown in S-Figure 8 of the Supporting Information. Two to three grams of the product can be obtained in a single preparation. Furthermore, the shape and size of the NC products can also be controlled by various reaction parameters, including the monomer concentration of metal precursors, type of precursors, and reaction time.

3.1. Synthesis of Rare Earth Oxide Nanocrystals. To date, a number of rare earth oxide nanocrystals are being studied intensively because of their diverse applications due to their unique 4f electrons,[25] including electronic, magnetic, optical, and catalytic fields. Many rare earth nanostructures have been synthesized through solution-based routes.[26] Among them, the hydrothermal two-phase route is particularly versatile for the synthesis of diverse rare earth oxide nanocrytals. However, this approach is rather restricted because metal alkoxides as precursors are commercially not available or expensive.

To overcome these drawbacks, in this work, we present two alternative two-phase routes to synthesize nanocrystalline rare

SCHEME 1: (A) Two-Phase Route to Synthesize Rare Earth Oxide Nanocrystals Using Rare Earth Salt Precursors and (B) Two-Phase Route to Synthesize Rare Earth Oxide Nanocrystals Using Rare Earth−Oleate Complex Precursors

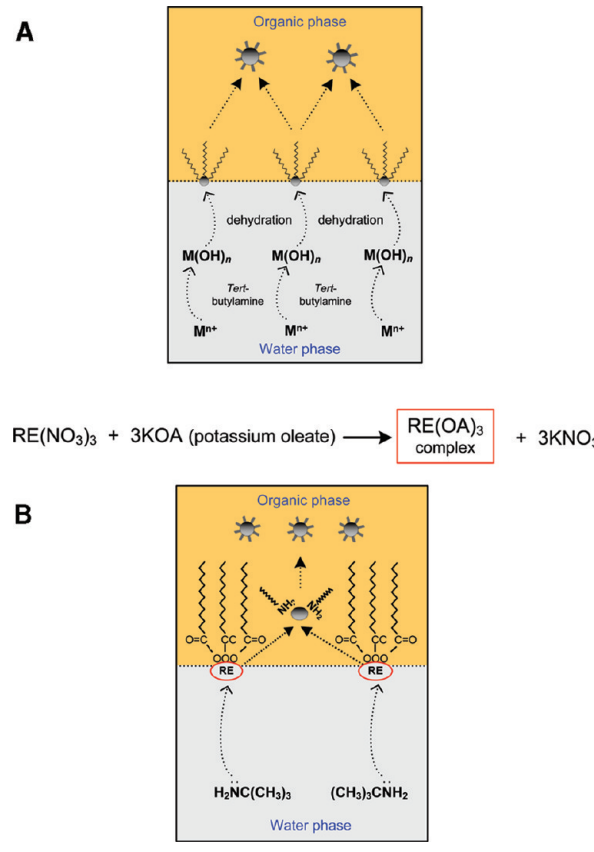

SCHEME 2: Two-Phase Route to Synthesize Transition Metal Oxide Nanocrystals Using Metal Salt Precursors

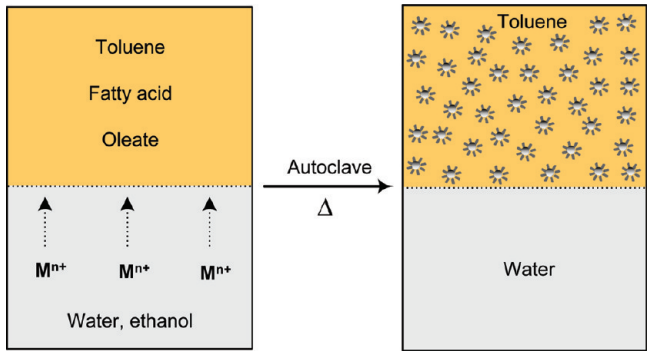

earth oxides in a water−toluene mixture in the presence of capping agents using (i) direct rare earth nitrate salts (Scheme 1A) and (ii) the rare earth−surfactant complexes prepared from the corresponding nitrate salts (Scheme 1B) as starting precursors.

3.1.1. Synthesis of Earth Oxide NCs Using Rare Earth Salt Precursors. Nanocrystalline rare earth oxides were obtained by the hydrolyzed reaction of the corresponding nitrate salts in a water−toluene mixture in the presence of capping molecules (fatty acid) and *tert*-butylamine (Experimental Section). This synthetic route shows the distinct advantage of relatively low temperature compared with the supercritical water method in the absence of *tert*-butylamine as an activation agent as reported by Adschiri et al.[22] Sm_2O_3 and CeO_2 were selected to illustrate this approach because they are widely recognized for their unique properties as supports and catalysts. The formation of rare earth oxide NCs is sketched in Scheme 1A.

In this way, the formation of Sm_2O_3 and CeO_2 NCs can be expressed in Scheme 1A. It is well-known that the Ce^{4+} ions have stable empty $4f^0$ subshells;[27] therefore, the Ce^{3+} ions were easily oxidized to the Ce^{4+} ions by the trace oxygen existing in the aqueous solution, according to the suggestion of Xing el al.[28] The metal hydroxides were formed under basic solution due to the hydrolysis of *tert*-butylamine in water to generate OH^- ions.[29] Upon hydrothermal treatment, these metal hydroxides were dehydrated to oxide nuclei at the interfaces.

Figure 1 shows the TEM images of Sm_2O_3 and CeO_2 NCs (samples 1 and 2 in Table 1) prepared at a high metal monomer concentration of the corresponding nitrate salts in the water solution (e.g., $C = 0.12$ M) following Scheme 1A. Under these synthesis conditions, single-crystalline Sm_2O_3 nanorods, ~7 nm in width and 100−160 nm in length (aspect ratio of ~19), were observed (Figure 1a); meanwhile, CeO_2 NCs composed of a mixture of nanocubes (6 nm) and elongated nanocubes (8 nm × 10 nm) were obtained. CeO_2 NCs had a tendency to assemble into 2D arrays (Figure 1c). The selected area electron diffraction (SAED) patterns taken by focusing the electronic beam on single samaria and ceria particles are presented in Figure 1b,d, respectively, showing the distinct diffraction rings of cubic structures, which is in good agreement with the XRD results (see below).

The size and shape evolution of CeO_2 NCs was found to be a function of cerium monomer concentrations, e.g., $Ce(NO_3)_3$, in the water solution. Representative TEM images of the samples are shown in Figure 2. At a relatively low cerium monomer concentration in the water phase ($C = 0.015$ M), only ordered CeO_2 nanocubes were formed with an average diameter of 3 nm (Figure 2a). However, their cube size increased from 3 to 8 nm when the cerium precursor concentration in the initial water phase was 0.068 M (Figure 2b). As observed under careful

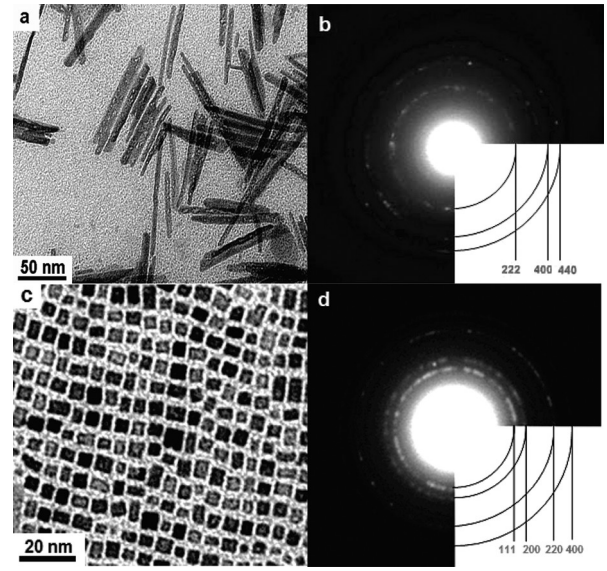

Figure 1. Rare earth oxide nanocrystals synthesized using corresponding nitrate salts at a high monomer concentration ($C = 0.120$ M) following Scheme 1A. (a) TEM image and (b) SAED pattern of 7 nm × 100−160 nm-sized Sm_2O_3 nanorods (sample 1). (c) TEM image and (d) SAED pattern of the CeO_2 NC mixture of 8 nm-sized nanocubes and 8 nm × 10 nm-sized elongated nanocubes (sample 2).

high-magnification TEM examination (inset of Figure 2b), the monodisperse nanocubes had strong tendency to assemble into multilayer superlattices (two-dimensional). By increasing the monomer concentration to 0.120 M, it yields some elongated nanocubes (8 nm × 10 nm) with sharper edges and corners. The self-assembly of the mixture of cubes and elongated cubes NCs was observed (Figure 2c). The general trend is also sketched in Figure 2d. The elongation and size of ceria nanocubes increased as the concentration of cerium monomers in the initial water solution increased. It is clear that the concentration of cerium salts plays an important role for the sizes and shapes of the resulting nanocubes. On the basis of the Gibbs−Thompson theory,[30] the chemical potential of a crystal is proportional to its surface−atom ratio; however, the size and shape evolution of NCs is strongly dependent on metal monomer concentrations as reported by Peng's group.[31,32] Generally, low monomer concentrations favor isotropic growth, whereas high monomer concentrations favor anisotropic growth.

Furthermore, the effect of the nature of cerium precursors on the size and shape of NCs was also studied. When cerium nitrate was replaced by cerium acetate ($C = 0.068$ M, acetate is weaker anion than nitrate[33,34]), some aggregated particles composed of two or three of the individual nanocubes with relatively larger sizes (8−10 nm) were observed (Figures 2e and 2f). This suggests that the nature of the counteranion ligands played a role in the growth of uniform nanocubes. Li et al.[33] also found that the variation of type of anion in the water phase could change the growth rate and, consequently, change the size and shape of Cu_2S nanocrystals.

Figure 3 shows the XRD patterns of the various calcined NC samples: Sm_2O_3 nanorods, CeO_2 nanocubes, and agglomerated CeO_2 nanocubes (samples 1, 2, and 3 in Table 1). The results revealed the body-centered cubic (*bcc*) structure of these samples with cell parameters for Sm_2O_3 of $a = 10.93$ Å (*Ia*3, JCPDS 86−2479) and for CeO_2 of $a = 5.45$ Å (*Fm*3*m*, JCPDS 34−0394). As seen in Figure 3, the XRD patterns show broad peaks due to the nanoscale size of the products, and no peaks of other impurities were detected. The sizes of these samples,

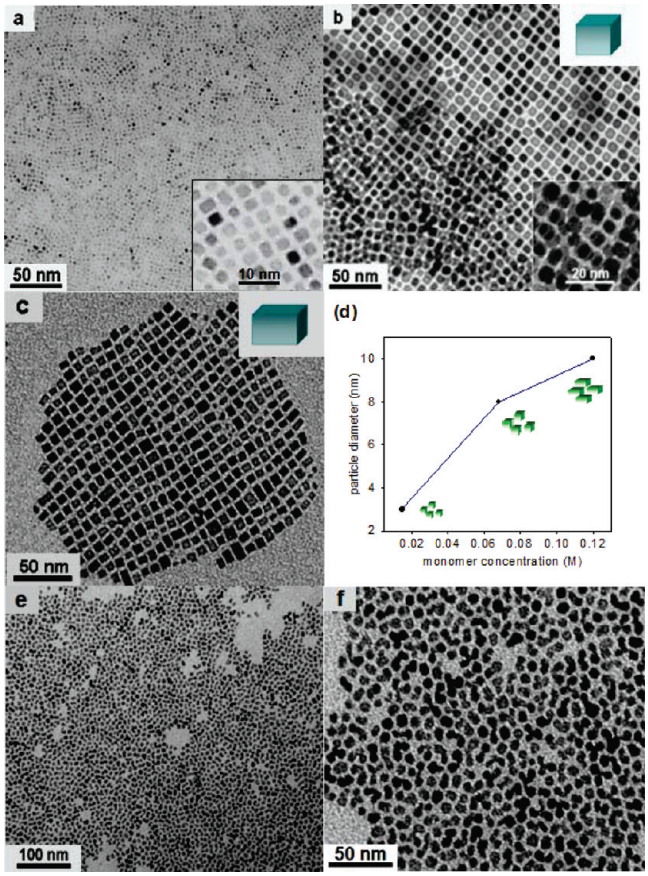

Figure 2. Shape and size evolution of CeO_2 nanocrystals as a function of cerium monomer concentrations (C). TEM images of CeO_2 NC samples prepared at (a) $C = 0.015$ M, 3 nm-sized nanocubes, (b) $C = 0.068$ M, 8 nm-sized nanocubes, and (c) $C = 0.120$ M, a mixture of 8 nm-sized nanocubes and 8 nm × 10 nm-sized elongated nanocubes. (d) Correlation plot showing the relationship of the cerium monomer concentration in a water phase and average diameter of CeO_2 nanocubes. (e,f) 8−10 nm-sized agglomerated CeO_2 nanocubes obtained using $Ce(ac)_3$ precursors ($C = 0.068$ M, sample 3).

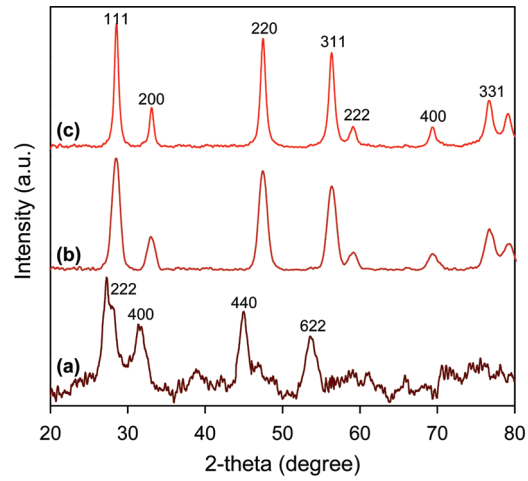

Figure 3. XRD patterns of the calcined rare earth oxide NC samples: (a) Sm_2 (sample 1), (b) CeO_2 NC mixture of nanocubes and elongated nanocubes (sample 2), and (c) agglomerated CeO_2 nanocubes (sample 3).

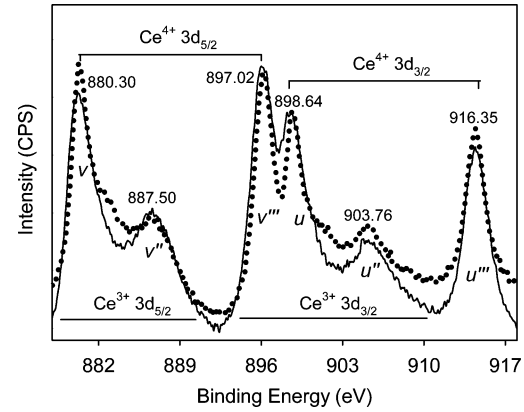

Figure 4. Ce 3d XPS spectra of the nanoceria (sample 2) before (solid curve) and after (dotted curve) calcination.

corresponding to samples 2 and 3 in Table 1 and calculated from the half-widths of the (220) reflections[35] using the Debye−Scherrer equation ($d = 0.89\lambda/B\cos\theta$), are ~11.0 and ~10.5 nm, respectively, which are consistent with the TEM results (S-Figure 9 of the Supporting Information).

The XPS spectra of metal oxides reveal that the metal core level binding energies and full widths at half-maximum (fwhm) taken from nanoparticles are obviously higher than those from the counterpart bulk.[36] The upward shift of binding energies by about 0.5−1.5 eV might result from the dispersion of metal ion clusters on the particle surfaces, while the increasing fwhm of about 2.5−3.5 eV might cause a change in electronic properties with decreasing particle size.[37]

The obtained cerium oxide NC products before and after calcination have a light yellow color, but pure bulk CeO_2 powders have a white color, indicating the chemical composition of cerium oxide NCs may be CeO_{2-x} ($0 < x < 2$). Replacement of the smaller Ce^{4+} ions (~0.92 Å radii) by a few larger Ce^{3+} ions (~1.034 Å radii) into the crystal lattice may result in the color change from white to light yellow. To further confirm this observation, we recorded the Ce 3d core level XPS spectra (Figure 4) for the sample of ceria nanocubes (solid curve) and after calcination (dotted curve, sample 2 in Table 1). The XPS spectra in wide energy ranges are also presented in S-Figure 1 of the Supporting Information; beside carbons, no impurities were found in this sample. It is interesting to note that no significant difference in the XPS spectrum before and after calcination of these samples was observed, suggesting no significant change in the cerium oxidation state with this thermal treatment. The Ce 3d states are split due to spin−orbit interaction into two lines: Ce $3d_{5/2}$/Ce $3d_{3/2}$ with a spin energy separation (Δ) of 18.3 eV and an intensity of $I(3d_{5/2})/I(3d_{3/2}) = 1.1$.[38] The complex spectrum of Ce 3d can be decomposed to six components with the assignment as defined in Figure 4. The bands at 887.50 eV (v'') and 903.76 eV (u'') are the $3d^{10}4f^1$ initial electronic state of the Ce^{3+} ion, and the bands at 880.30 eV (v'), 887.50 eV (v''), 887.50 eV (v'''), 898.64 eV (u), 903.76 eV (u''), and 916.35 eV (u''') are the $3d^{10}4f^0$ state of the Ce^{4+} ion.[37] The atomic ratio of $Ce^{3+}/(Ce^{3+} + Ce^{4+})$ of the as-made and calcined ceria NC samples can be quasi-quantitatively determined by the ratio of $(I_{v''} + I_{u''})/(I_u + I_v + 2I_{v''} + 2I_{u''} + I_{v'''} + I_{u'''})$, which is ~46%. Furthermore, the Ce/O ratio was found to be 1.00:1.67, corresponding the stoichiometric formula of CeO_{2-x} ($x = 0.33$). This suggests that the distorted crystal structure of nanoceria due to the replacement of Ce^{4+} ions by Ce^{3+} ions causes an oxygen vacancy creation in surface defects. The presence of two oxidation states (Sm^{2+}/Sm^{3+}) with 40% Sm^{2+} and the chemical composition of $Sm_2O_{(3-1.8)}$ on the samaria NC surface were observed in our recent study.[24]

3.1.2. Synthesis of Rare Earth Oxide NCs Using Rare Earth−Surfactant Complex Precursors. Recently, we have reported the shape selective synthesis of vanadium oxide nanocrystals (NCs) through the decomposing of vanadium−ligand complexes in the water−toluene mixture in the presence of aliphatic amine.[17] It was found that the size and shape of NCs can be controlled by various synthesis parameters such as water content, steric ligands of vanadium complexes, and the alkyl chain length of capping agents. Some authors had developed the two-phase method to produce the semiconductor nanocrystals.[39] However, few reports described a general route for rare earth oxide nanocrystal synthesis as well as studies of the reaction mechanism. From these points of view, we extend into a general method and study of the reaction mechanism for the synthesis of different types of rare earth oxide nanocrystals (REO-NCs) using rare earth−oleate complexes. In this work, Er, Gd, La, and Y oxide NCs were selected and synthesized with controllable size and shape because of their wide variety of technological applications and limited information available in the literature for the synthesis of these NCs through two-phase approach.[18]

The synthesis of REO-NCs involves two steps (Scheme 1B): (i) the preparation of rare earth−oleate complexes from the reaction between rare earth nitrate and potassium oleate (KOA) in a water−toluene system and (ii) the formation of colloidal REO-NCs in the autoclave containing the water−toluene mixture composed of capping oleylamine, *tert*-butylamine, and rare earth−oleate complexes at 180 °C. All of the rare earth−oleate complexes (Er, Gd, La, and Y) were synthesized from the corresponding rare earth nitrate compounds using the same procedure. For example, the FTIR spectrum of the Y−oleate complex precursor (after toluene elimination) is shown in S-Figure 2 of the Supporting Information. The absorption band at 731 cm^{-1} is assigned to the stretching vibrations of the Y−O bonds.[40] Two absorption bands are observed at 1466 cm^{-1} and 1548 cm^{-1}, which are attributed to the symmetric and asymmetric stretching vibrations of the carboxylate groups of oleate ligands, respectively. The strong absorption bands at 2849−2928 cm^{-1} are characteristic of the symmetric and asymmetric methyl and methylene stretches of the alkyl chains. These FTIR bands are characteristic of Y−oleate complexes.[41]

The rare earth nanocrystals (RE-NCs) synthesized with different morphologies are summarized in Table 1. To prove as-made RE-NCs are protected by oleylamine molecules, a representative FTIR spectrum of the OM-capped Y_2O_3 sample is presented in S-Figure 3a of the Supporting Information. It clearly indicates oleylamine molecules bonded on the nanocrystal surface. Figure 5 shows the XRD patterns of various types of calcined NC products. The Er_2O_3, Gd_2O_3, and Y_2O_3 samples exhibit cubic structures, while the La_2O_3 sample shows a hexagonal structure. The calculated lattice constants are 10.63, 11.28, 10.80, 10.56, and 3.39 Å for Y_2O_3 (JCPDS 25-1200),[41] Gd_2O_3 (JCPDS 86-2477),[42] Er_2O_3 (JCPDS 08-0050),[43] and La_2O_3 (JCPDS 05-0602), respectively.[44] The particle sizes of Gd_2O_3 and Er_2O_3 NCs calculated from the (222) reflections are about 20 and 30 nm, respectively, which are consistent with the sizes obtained by the TEM images (see below and S-Figure 9 of the Supporting Information). The XRD spectra of all of the nanocrystal samples show much broader diffraction peaks compared to those of their bulk counterparts because of their nanometer size.

It should be noted that *tert*-butylamine and rare earth−oleate complexes play a key role for the formation of rare earth nanocrystals. For example, the synthesis of Y_2O_3 NCs was carried out under the same synthesis conditions, and except for the absence of *tert*-butylamine in the synthesis mixture, no rare earth NC product was formed. When yttrium acetate compounds were used instead yttrium−oleate complexes, keeping the other synthesis conditions constant (e.g., in the presence of capping oleylamine and *tert*-butylamine), only irregular Y_2O_3 nanospheres were obtained (S-Figure 4 of the Supporting Information).

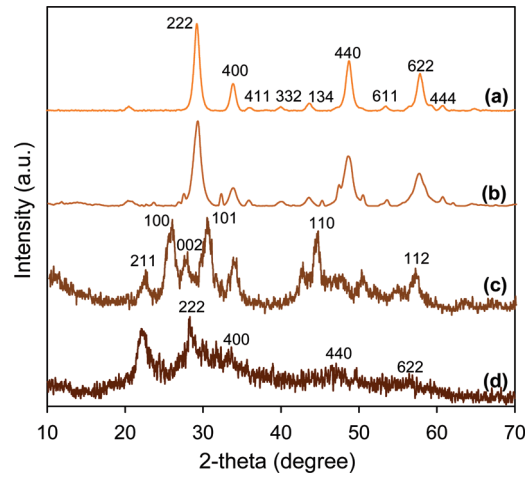

Figure 5. XRD patterns of calcined rare earth oxide NC samples synthesized using corresponding rare earth−oleate complexes following Scheme 1B: (a) Er_2O_3 nanospheres (sample 4), (b) Y_2O_3 nanorods (sample 7), (c) La_2O_3 nanorods (sample 6), and (d) Gd_2O_3 nanospheres/nanopeanuts (sample 5).

The formation of NCs using rare earth−oleate complexes, capping oleylamine, and *tert*-butylamine could be expressed in eq 1. The formation of RE-NCs could consist of three steps during the hydrothermal synthesis: (i) *Tert*-butylamine as nucleophile attacks one carboxyl group of the oleate ligand through the sharing of a lone pair of electrons of the donor NH_2 group with the electrophilic carboxyl center at the nucleation stage. *Tert*-butylamine can react with the oleate group but not with oleylamine because its basic property is stronger than that of oleylamine. Moreover, *tert*-butylamine is dispersed an aqueous phase and easily hydrolyzed to generate OH^- compared with oleylamine in organic phase. (ii) This nucleophilic reaction leads to C−O bond cleavage, the release of a carbonyl group, and then the formation of REO nuclei at the water−toluene interfaces. (iii) The formation of NCs. A similar observation was also reported for the synthesis of ZnO nanocrystals in the mixture of zinc acetate and oleylamine.[45]

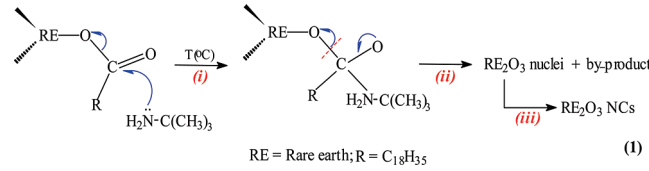

Figures 6−8 show representative TEM images and SAED patterns of different rare earth oxide NCs (Table 1). Under the same synthesis conditions, different shapes of the final NC products were observed: spheres for Er_2O_3 (Figure 6), the mixture of spheres and peanuts for Gd_2O_3 (Figure 7), and rods for La_2O_3 and Y_2O_3 (Figure 8), depending on metal−oleate complexes. Er_2O_3 nanospheres with a size of about 10−20 nm were obtained, meaning that no growth direction is dominant during the seeded growth, whereas nanorods were yielded for

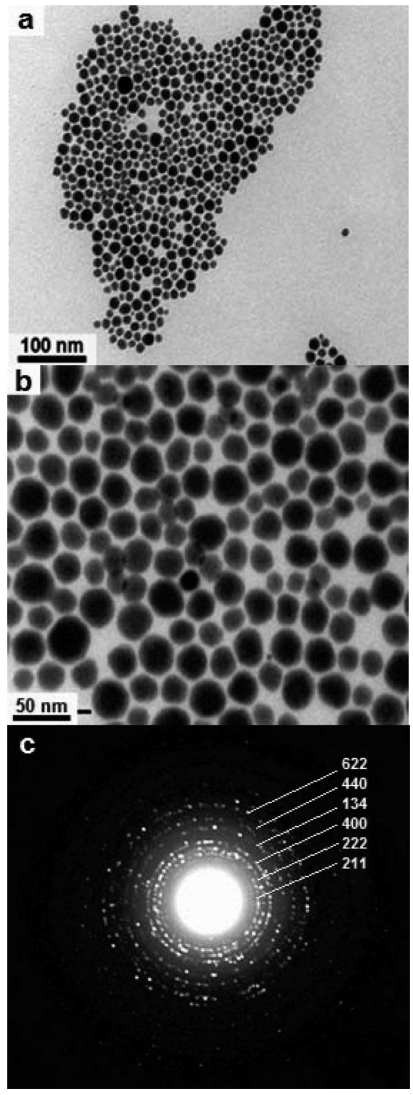

Figure 6. TEM images and corresponding SAED pattern of Er_2 synthesized using Er−oleate complexes.

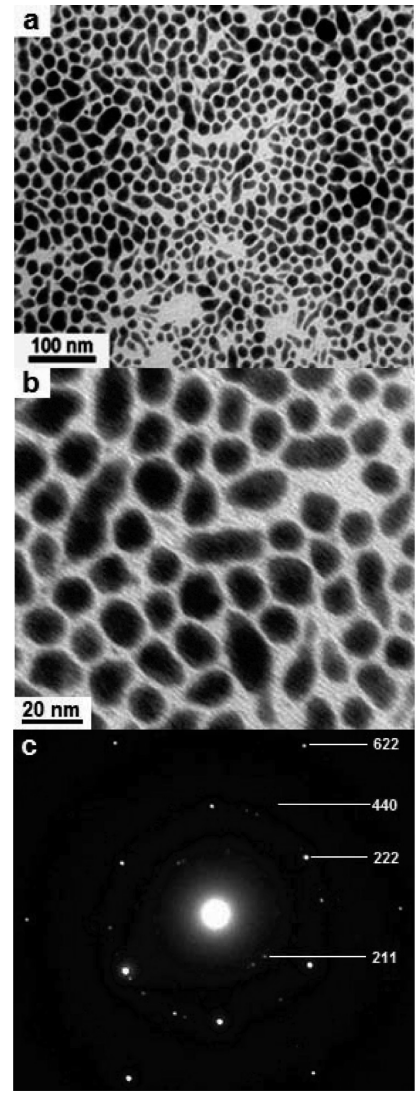

Figure 7. TEM images and corresponding SAED pattern of Gd_2O_3 nanospheres/nanopeanuts synthesized using Gd−oleate complexes.

La_2O_3 and Y_2O_3. The La_2O_3 nanorods of 8 nm in width and 20 nm in length with an aspect ratio of ∼2.5 were observed, while Y_2O_3 nanorods (10 nm × 80−120 nm) with the aspect ratio of ∼10 were observed. However, for Gd_2O_3, the mixture of nearly round-shaped nanocrystals (10−20 nm) and partly nanopeanuts (10−20 nm × 20−40 nm) was identified. The corresponding SAED patterns of these Er_2O_3, Gd_2O_3, and Y_2O_3 NC samples exhibit a set of sharp spots that are characteristic of single crystalline cubic structures, while the diffraction rings of the La_2O_3 NC sample corresponds to a hexagonal structure, which is in good agreement with the XRD results.[41−44] It seems that unit cell structure and crystallographic surface energy of seeds are critical for directing the intrinsic shapes of rare earth oxide NCs (Figure 8d).

Survey XPS spectra were recorded for these samples. The XPS spectra of the calcined Y_2O_3 nanorods are shown in S-Figures 5 of the Supporting Information. As seen in Figure 5A, no significant presence of impurities was observed, except for the carbon. The XPS spectrum of Y 3d (S-Figure 5B of the Supporting Information) shows only the Y $3d_{5/2}$ and Y $3d_{3/2}$ peaks centered at 151.55 and 153.47 eV, respectively, which are attributed to Y^{3+}.[46] It suggests only one yttrium oxidation state in the yttrium oxide NC sample after calcination. The atomic ratio of Y:O determined from the surface chemical composition of this sample was 1.05:1.51, corresponding to Y_2O_3. The surface chemical compositions for other calcined NC samples are found to be Er_2O_3, Gd_2O_3, and La_2O_3 (not shown).

The mesoporous structure of Er_2O_3 nanospheres and Gd_2O_3 nanospheres/nanopeanuts after calcination at 550 °C for 2 h were examined by N_2 sorption measurements (S-Figure 6 of the Supporting Information). The isotherm of both samples is type IV with an H1 hysteresis loop.[24,47] These calcined Er_2O_3 and Gd_2O_3 samples have a BET surface area of 55 and 35 m^2/g, respectively, and average pore diameters of 28 and 18 nm, respectively. The pore size distribution of the Gd_2O_3 sample (inset of S-Figure 6B of the Supporting Information) shows a bimodal pore structure. The bimodal pore size distribution may due to the slit-shaped pores of the mixture of nanospheres and nanopeanuts.

3.2. Synthesis of Transition Metal Oxide Nanocrystals (TMO-NCs). Transition metal oxides have been widely used in many applications, especially for catalysis and fuel cell technology. In addition, size and shape of these materials provide a sensitive knob for tuning their properties.[48] A number of chemical routes have been developed to produce nanocrystals of transition metal oxides with defined and controllable shapes.[49] In most cases, nanocrystals were formed at high temperatures. Therefore, the development of approaches for the synthesis of

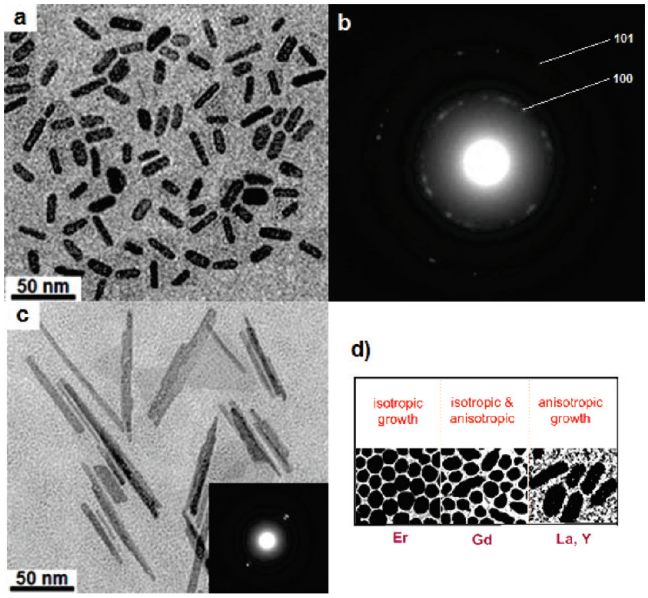

Figure 8. TEM images and corresponding SAED patterns of the rare earth oxide nanocrystals synthesized using the corresponding rare earth−oleate complexes: (a,b) La_2O_3 nanorods and (c) Y_2O_3 nanorods. (d) Growth diagram of RE_2O_3 NCs (RE = Er/Y).

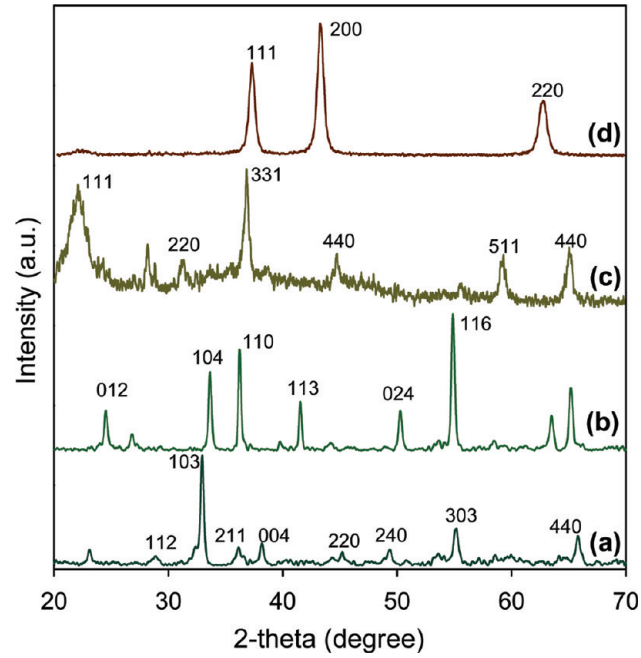

Figure 9. XRD patterns of the calcined transition metal oxide NC samples: (a) hexagonal Mn_3O_4 nanocrystals (sample 8), (b) Cr_2O_3 nanodots (sample 9), (c) Co_3O_4 nanospheres (sample 10), and (d) hexagonal NiO nanocrystals (sample 13).

such nanocrystals under mild reaction conditions with size and shape control remains a challenge. We developed a new procedure for the synthesis of a large variety of monodisperse transition metal oxide nanocrystals through a hydrothermal two-phase approach at relatively low temperature (150−180 °C) using inexpensive compounds such as transition metal salts and potassium oleate, instead of expensive organometallic compounds. The synthetic procedure is illustrated in Scheme 2. The biphasic mixture was composed of an aqueous phase of metal ion (e.g., metal nitrate or chloride), ethanol, and water and a toluene phase of potassium oleate and oleic acid. The metal−oleate complex was directly formed in a water−toluene mixture from an ion exchange reaction of a metal cation with an oleate anion in an early mass transfer stage: $M^{n+} + nRCOO^- \rightarrow M(COOR)_n$.[50] Under hydrothermal synthesis conditions, the resulting metal−oleate complexes were reduced by ethanol to generate tiny oxide nuclei at the interfaces and then form metal oxide nanocrystals, which were capped by fatty acid in an organic phase; no NC product was observed in an aqueous phase. To describe this approach, we selected four different transition-metal oxides (Mn_3O_4, Cr_2O_3, Co_3O_4, and NiO) and to synthesize in this study (Table 1). FTIR measurements were carried out for of these as-made OA-capped TMO-NCs. A representative FTIR spectrum of the as-made OA-capped Co_3O_4 NC sample (sample 10) is shown in S-Figure 7b of the Supporting Information. The presence of the FTIR bands correspond to the stretching frequency of the carboxylate groups from the oleic acid, indicating that these groups were bonded to the NC surface. As seen in Figure 9, the XRD patterns of these samples are well-matched to tetragonal Mn_3O_4 (JCPDS 16-0154) with $a = 5.759$ Å,[51] rhombohedral Cr_2O_3 (JCPDS 05-0667) with $a = 4.958$ Å;[52] cubic Co_3O_4 (JCPDS 48-1719) with $a = 8.084$ Å,[53] and cubic NiO (JCPDS 04-0835) with $a = 4.193$ Å.[54] A broadening of XRD peaks indicates the nanocrystalline nature of these samples. Furthermore, no other phases were detected in the spectra, suggesting the pure structure of the products. The particle sizes calculated using the Scherrer equation from the (103), (110), (331), and (200) reflections for Mn_3O_4, Cr_2O_3, Co_3O_4, and NiO NCs, respectively, were about 12, 7, 5, and 7 nm, which are consistent with the TEM results (S-Figure 9 of the Supporting Information).

Representative TEM images and SAED patterns of these samples are shown in Figure 10. The Mn_3O_4 and NiO NCs exhibit a hexagonal-like shape with an average diameter of nearly 10 and 8 nm, respectively. Closer TEM observation of the Mn_3O_4 NC sample shows single hexagon self-assembled two-dimensional (2D) networks. The Cr_2O_3 NC sample shows self-assembled nanodots with an average diameter of about 3 nm. Furthermore, 6 nm-sized nanospheres and a few truncated nanospheres of Co_3O_4 prefer to construct the ordered hexagonal self-assembly, as proposed by the simulation in the inset of Figure 10e. The corresponding SAED patterns of these Mn_3O_4, NiO, Cr_2O_3, and Co_3O_4 NC samples exhibit strong diffraction rings and can be well-indexed to tetragonal, cubic, rhombohedral, and cubic structures, respectively.

The self-assembly of Co_3O_4 nanocubes into nanospheres was also observed (Figure 11) as a function of reaction time when all of the synthesis conditions were kept constant (e.g., cobalt nitrate, solvent volume, potassium oleate, oleic acid, and reaction temperature corresponding to 0.08 M, 40 mL, 3 g, 2 mL, and 180 °C, respectively). During the crystal growth process, the capping surfactant plays an important role in the size and shape of the nanoparticles. In this study, oleic acid was used as a capping agent, and its concentration was fixed in the reaction solution. After heating at 180 °C for a relatively short time, 12 h, the TEM image of this sample shows two populations of particles sizes (Figure 11a): polydisperse small nanocubes (2−4 nm) and relatively monodisperse nanocubes self-assembly (∼5 nm). However, after 18 h of synthesis, relatively uniform nanocrystals with an average size of 6 nm were observed (Figure 11b). Furthermore, when the synthesis time was extended to 24 h, the morphology of the product was remarkably changed. The corners and tips of cubes gradually became smooth, and monodisperse spherial nanocrystals were formed (Figure 11c). These results indicate that a transformation of the nanocubes to monodisperse 6 nm-sized nanospherical self-assembly occurs

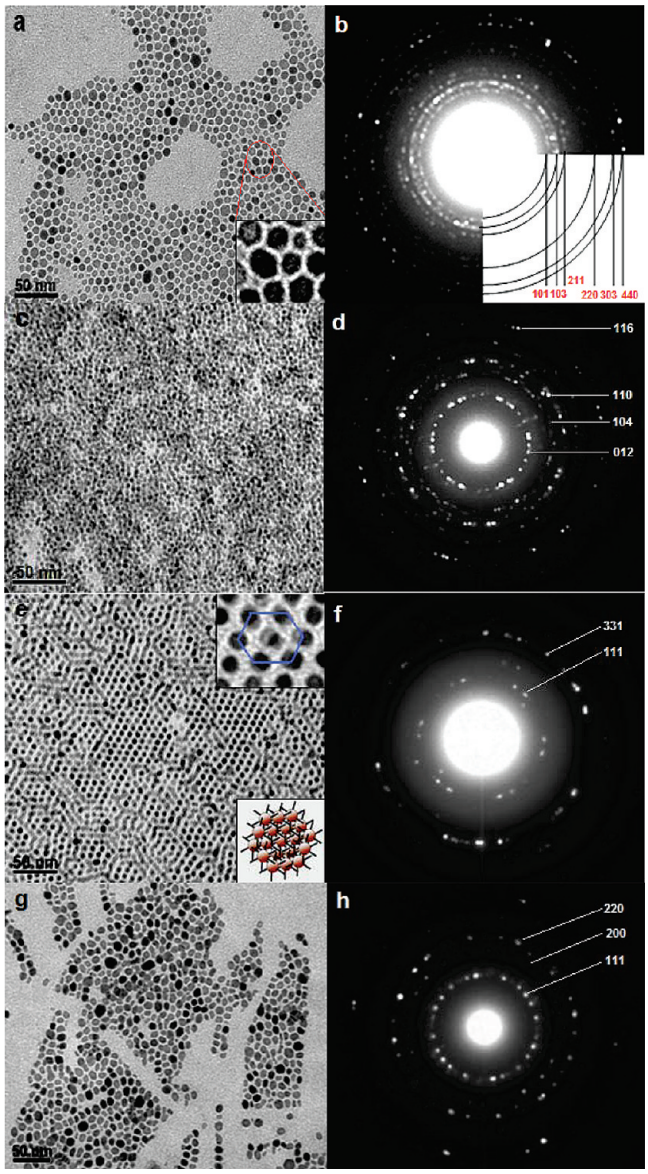

Figure 10. TEM images and corresponding SAED patterns of transition metal oxide nanocrystals synthesized using the corresponding metal salts following Scheme 2: (a,b) 10 nm-sized hexagonal Mn_3O_4 nanocrystals, (c,d) 3 nm-sized Cr_2O_3 nanodots, (e,f) 6 nm-sized nanospheres and a few truncated nanospheres of Co_3O_4, and (g,h) 8 nm-sized hexagonal NiO nanocrystals.

with an extended reaction time, as suggested in Figure 11d. The most commonly used model for shape control is the Gibbs−Curie−Wulff facet theorem,[55,56] which suggests that the shape of a crystal is determined by the minimum surface energy of each facet of the crystal. This means that crystal growth should occur rapidly at high free energy facets. In the early stages, Co_3O_4 nanocubes can be formed in anisotropic growth. Nanocubes enclosed by six crystal faces of {100}, {010}, and {001} were formed by the specific growth of {111} facets of the cuboctahedral clusters. This also indicates that the {111} surface has a higher surface energy compared to the {100}, {010}, and {001} surfaces.[57,58] When extending the reaction time, the monomer Co(II)−oleate complex concentration was gradually depleted by the nucleation and growth of the nanocrystals. If the reaction time is sufficiently long (in this case, 24 h), the monomer concentration should drop to a level that is a lower than that required for a given cubic shape. The cubic shape should eventually evolve into the spherical shape, which is most stable

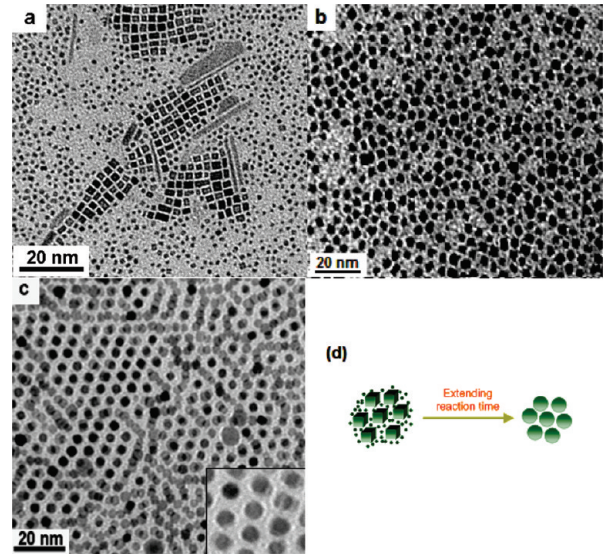

Figure 11. TEM images of Co_3 times: (a) 12 h, a mixture of nanocubic and nanocubic self-assemblies (sample 12), (b) 18 h, nanocubes (sample 11), (c) 24 h, self-assemblied nanospheres nanospheres (sample 10). (d) A suggested scheme for the self-assembly of a spherical shape.

shape, by moving monomers from {111} to {100} faces in intraparticles due to the differences in chemical potential between different facets of the nanocrystals. In this case, a few truncated nanospheres were still observed. This may be due to the insufficient ripening reaction time for the transformation of cubes to spheres.

These NC samples, manganese oxide, cobalt oxide, and chromium oxide nanocrystals before and after calcination, were characterized by the XPS technique (Figure 12 and S-Figure 7 of the Supporting Information). The XPS spectra before (solid curve) and after (dotted curve) calcination of these samples are almost indentical, suggesting no significant change in the oxidation state upon this thermal treatment (Figure 12). The deconvolution results of the Mn 2p, Co 2p, and Cr 2p peak XPS spectra are shown in Figures 12A, 12B, and 12C, respectively. The Mn $2p_{3/2}$ peaks are centered at ~640.59−652.01 eV, and Mn $2p_{1/2}$ peaks are centered at ~642.20−653.60 eV, with $\Delta \approx 1.6$ eV, indicating those of pure Mn_3O_4 phase.[59] The O 1s peaks (not shown) were located at 529.76−531.76 eV and are assigned to oxygen in Mn_3O_4. The other shoulder at 533.40 eV is attributed to the presence of a hydroxyl species or adsorbed water on the surface.

For the cobalt oxide NC sample, the two main Co 2p binding energies are ~779.63−794.85 eV (Co $2p_{3/2}$), ~781.70−796.35 eV (Co $2p_{1/2}$), and $\Delta \approx 2.1$ eV, and the shakeup satellites (I) with a low intensity at ~10.6 eV due to the main Co 2p band are characteristic of those of pure Co_3O_4.[60] The shakeup satellites (II) at ~5.6 eV from the weak Co 2p bands suggests the presence of NC surface hydroxyls. The Cr 2p spectrum of the chromium oxide NC sample shows the Cr $2p_{3/2}$ peak at 576.88−586.39 eV, and the Cr $2p_{1/2}$ peaks at 579.74−588.91 eV are attributed to Cr^{3+}.[61] The O 1s peak (not shown) is often believed to be composed of two peaks, related to two different chemical states of oxygen. The binding energies of each individual component are 531.80 (Cr^{3+}-O) and 533.35 eV (OH^-). Furthermore, the calculated atomic ratios of Mn:O, Co:O, and Cr:O are found to be very close to 0.73:1.00, 0.85:1.00, and 0.98:1.49, respectively, corresponding to the stoichiometry of Mn_3O_{4-x} ($x = 1.25$), Co_3O_{4-x} ($x = 1.47$), and Cr_2O_3, respectively.

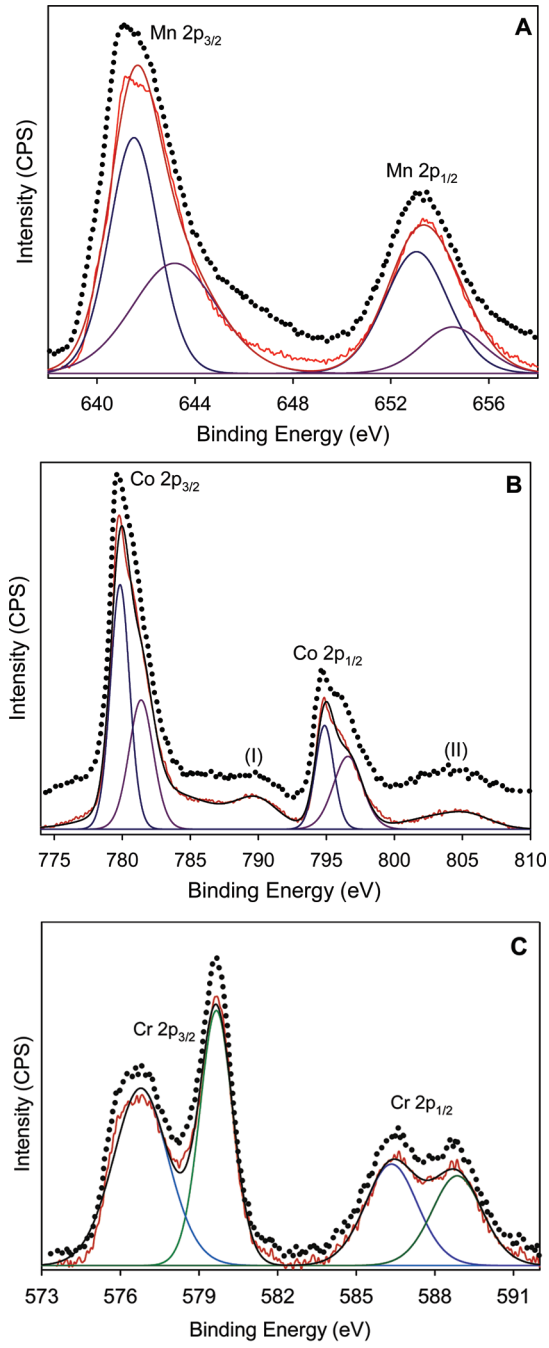

Figure 12. High-resolution XPS spectra of the transition metal oxide NC samples before (solid curve) and after (dotted curve) calcination: (A) Mn 2p core level for hexagonal Mn_3O_4 nanocrystals (sample 8), (B) Co 2p core level for Co_3O_4 nanospheres (sample 10), and (C) Cr 2p core level for Cr_2O_3 nanodots (sample 9).

4. Conclusion

Different two-phase methods have been developed for the synthesis of two classes of monodisperse metal oxide nanocrystals: rare earth oxides and transition metal oxides, using metal salts as starting precursors instead of expensive organometallic compounds. The results revealed that for the formation of rare earth oxide nanocrystals, *tert*-butylamine plays a key role as a nucleophile agent. However, in the case of transition metal oxide nanocrystals, ethanol is an important agent for reducing the monomeric transition metal precursors to induce NC products. Various sizes and shapes of monodisperse nanoparticles such as cubic, spherical, hexagonal, peanut, and rod NCs were obtained depending on the nature of metal precursors. The size and shape evolution of CeO_2 NCs was found to be as a function of monomer concentration of cerium salts. The size and shape varied from 3 nm-sized cubes to 8 nm × 10 nm-sized elongated cubes, when the cerium monomer concentration increased from 0.015 to 0.120 M. This could be related to increasing the chemical potential in bulk solution. In the case of Co_3O_4 nanocrystals, the morphology changed from nanocube to nanospheres, when the reaction time increased from 12 to 24 h at 180 °C, due to the differences in chemical potential between different facets of the nanocrystals.

The SAED patterns of the obtained NC samples show a set of sharp spots characteristic of single crystalline structures, and the strong diffraction rings indexed accordingly with the structures determined by the XRD spectra. The XPS results revealed the presence of two oxidation states of cerium, samarium, manganese, and cobalt on the nanocrystal surface. However, it seems that only one oxidation state on the surface for Y, Cr, and La oxide nanocrystals is present. Two different components of the O 1s XPS large peak for these Ce, Sm, Mn, and Co oxide NC samples refer to the defected structure.

These synthetic methods have several advantages, including relatively mild conditions, easy manipulation with controllable size and shape of the NCs, and a possibilty to scale-up to the multigram-scale products using inexpensive metal salt precursors. These methods can be extended to the synthesis of other uniform NCs as well as doped and multicomponent NCs. Further work is in progress in our laboratory.

Acknowledgment. This work was supported by the Natural Sciences and Engineering Research Council of Canada (NSERC) through a strategic grant. The authors thank Profs. S. Kaliaguine and F. Kleitz for stimulating discussions and comments.

Supporting Information Available: XPS spectra of the CeO_2 nanocubic sample, TEM images of the as-synthesized metal oxide nanocrystals after calcination, TEM images of the alkyl chain-capped metal oxide nanocrystals synthesized as multigram-scale products, XPS spectra in the wide-energy range of the transition metal oxide NC samples, FTIR spectrum of the Y−oleate complex precursor, FTIR spectra of alkyl-capped metal oxide NCs, TEM image of as-made Y_2O_3 nanocrystals, N2 adsorption−desorption isotherms and corresponding pore size distribution curves. This material is available free of charge via the Internet at http://pubs.acs.org.

References and Notes

(1) Jun, Y. W.; Seo, J. W.; Cheon, A. J. *Acc. Chem. Res.* **2008**, *41*, 179–189.
(2) El-Sayed, M. A. *Acc. Chem. Res.* **2004**, *37*, 326–333.
(3) Garcia, M. F.; Arias, A. M.; Hanson, J. C.; Rodriguez, J. A. *Chem. Rev.* **2004**, *104*, 4063–4104.
(4) Wang, X.; Peng, Q.; Li, Y. *Acc. Chem. Res.* **2007**, *40*, 635–643.
(5) Kinge, S.; Calama, M. C.; Reinhoudt, D. N. *ChemPhysChem* **2008**, *9*, 20–42.
(6) Rao, C. N. R.; Kulkarni, G. U.; Thomas, P. J.; Edwards, P. P. *Chem.—Eur. J.* **2002**, *8*, 28–35.
(7) Daniel, M. C.; Astruc, D. *Chem. Rev.* **2004**, *104*, 293–346.
(8) Niederberger, M.; Garnweitner, G.; Buha, J.; Polleux, J.; Ba, J.; Pinna, N. *J. Sol−Gel Sci. Technol.* **2006**, *40*, 259–266.
(9) Wang, X.; Li, Y. *Chem. Commun.* **2007**, 2901–2910.
(10) Kwon, S. G.; Hyeon, T. *Acc. Chem. Res.* **2008**, *41*, 1696–1709.
(11) Redl, F. X.; Cho, K. S.; Murray, C. B.; O'Brien, S. *Nature* **2003**, *423*, 968–971.
(12) Yin, Y.; Alivisatos, A. P. *Nature* **2004**, *437*, 664–670.
(13) Brust, M.; Walker, M.; Bethell, D.; Schiffrin, D. J.; Whyman, R. *J. Chem. Soc., Chem. Commun.* **1994**, 801–802.
(14) Xia, Y.; Xiong, Y.; Lim, B.; Skrabalak, S. E. *Angew. Chem., Int. Ed.* **2009**, *48*, 60–103.

(15) Pan, D.; Wang, Q.; Jiang, S.; Ji, X.; An, L. *Adv. Mater.* **2005**, *17*, 176–179.
(16) Pan, D.; Ji, X.; An, L.; Lu, Y. *Chem. Mater.* **2008**, *20*, 3560–3566.
(17) Nguyen, T. D.; Do, T. O. *Langmuir* **2009**, *25*, 5322–5332.
(18) Pan, D.; Wang, Q.; An, L. *J. Mater. Chem.* **2009**, *19*, 1063–1073.
(19) Pan, D.; Zhao, N.; Wang, Q.; Jiang, S.; Ji, X.; An, L. *Adv. Mater.* **2005**, *17*, 1991–1995.
(20) Zhao, N. N.; Pan, D. C.; Nie, W.; Ji, X. L. *J. Am. Chem. Soc.* **2006**, *128*, 10118–10124.
(21) Du, H.; Wohlrab, S.; Weiss, M.; Kaskel, S. *J. Mater. Chem.* **2007**, *17*, 4605–4610.
(22) Zhang, J.; Ohara, S.; Umetsu, M.; Naka, T.; Hatakeyama, Y.; Adschiri, T. *Adv. Mater.* **2007**, *19*, 203–206.
(23) Mrabet, D.; Zahedi-Niaki, M. H.; Do, T. O. *J. Phys. Chem. C* **2008**, *112*, 7124–7129.
(24) Nguyen, T. D.; Mrabet, D.; Do, T. O. *J. Phys. Chem. C* **2008**, *112*, 15226–15235.
(25) Jun, Y. W.; Choi, J. S.; Cheon, J. *Angew. Chem., Int. Ed.* **2006**, *45*, 3414–3439.
(26) Yan, Z. G.; Yan, C. H. *J. Mater. Chem.* **2008**, *18*, 5046–5059.
(27) Cotton, F. A.; Wilkinson, G.; Murillo, C. A.; Bochmann, M. *Advanced Inorganic Chemistry*, 6th ed.; John Wiley & Sons: New York, 1999.
(28) Yan, L.; Yu, R.; Chen, J.; Xing, X. X. *Cryst. Growth & Des.* **2008**, *8*, 1474–1477.
(29) Knifton, J. F.; Grice, N. J. *Tert*-butylamine Synthesis over Montmorillonite Clays. U.S. Patent 5304681, 1994.
(30) Rottman, C.; Voorhees, P. W.; Johnson, W. C. *Scripta Metallurgica* **1988**, *22*, 293–298.
(31) Peng, Z. A.; Peng, X. G. *J. Am. Chem. Soc.* **2002**, *124*, 3343–3353.
(32) Peng, X. G. *Adv. Mater.* **2003**, *15*, 459–463.
(33) Zhuang, Z.; Peng, Q.; Zhang, B.; Li, Y. *J. Am. Chem. Soc.* **2008**, *130*, 10482–10483.
(34) Wu, Q.; Zhang, F.; Xiao, P.; Tao, H.; Wang, X.; Hu, Z. *J. Phys. Chem. C* **2008**, *112*, 17076–17080.
(35) Taniguchi, T.; Watanabe, T.; Sakamoto, N.; Matsushita, N.; Yoshimura, M. *Cryst. Growth Des.* **2008**, *8*, 3725–3730.
(36) Alivisatos, A. P. *J. Phys. Chem.* **1996**, *100*, 13226–13239.
(37) Kapteijn, F.; Langeveld, A. D. V.; Moulijn, J. A.; Andreini, A.; Vuurman, M. A.; Turek, A. M.; Jehng, J. M.; Wachs, I. E. *J. Catal.* **1994**, *150*, 94–104.
(38) Zhang, F.; Wang, P.; Koberstein, J.; Khalid, S.; Chan, S. C. *Surf. Sci.* **2004**, *563*, 74–82.
(39) Wang, Q.; Pan, D.; Jiang, S.; Ji, X.; An, L.; Jiang, B. *Chem.—Eur. J.* **2005**, *11*, 3843–3848.
(40) Yongiu, L.; Xiaoyun, L.; Yizheng, W.; Junming, L.; Weili, S. *J. Rare Earths* **2006**, *24*, 34–38.
(41) Nelson, J. A.; Wagner, M. J. *Chem. Mater.* **2002**, *14*, 915–917.
(42) Soderlind, F.; Pedersen, H.; Petoral Jr, R. M.; Kall, P. O.; Uvdal, K. *J. Colloid Interface Sci.* **2005**, *288*, 40–148.
(43) Han, K.; Zhang, Y.; Fang, Z.; Cheng, T.; Gao, M. *Chem. Lett.* **2007**, *36*, 1124–1125.
(44) Murugan, A. V.; Navale, S. C.; Ravi, V. *Mater. Lett.* **2006**, *60*, 848–849.
(45) Zhang, Z.; Lu, M.; Xu, H.; Chin, W. S. *Chem.—Eur. J.* **2007**, *13*, 632–638.
(46) Van, T. T.; Chang, J. P. *Surf. Sci.* **2005**, *596*, 1–11.
(47) Tuysuz, H.; Liu, Y.; Weidenthaler, C.; Schuth, F. *J. Am. Chem. Soc.* **2008**, *130*, 14108–14110.
(48) Thomas, J. M.; Simpson, E. T.; Kasama, T.; Borkowski, R. E. D. *Acc. Chem. Res.* **2008**, *41*, 665–674.
(49) Park, J.; Joo, J.; Kwon, S. G.; Jang, Y.; Hyeon, T. *Angew. Chem., Int. Ed.* **2007**, *46*, 4630–4660.
(50) Park, J.; An, K.; Hwang, Y.; Park, J. G.; Noh, H. J.; Kim, J. Y.; Park, J. H.; Hwang, N. M.; Hyeon, T. *Nat. Mater.* **2004**, *3*, 891–895.
(51) Lei, S.; Tang, K.; Fang, Z.; Zheng, H. *Cryst. Growth Des.* **2006**, *6*, 1757–1760.
(52) Li, L.; Yan, Z. F.; Lu, G. L.; Zhu, Z. H. *J. Phys. Chem. B* **2006**, *110*, 178–183.
(53) Kumar, U.; Shete, A.; Harle, A. S.; Kasyutich, O.; Schwarzacher, W.; Pundle, A.; Poddar, P. *Chem. Mater.* **2008**, *20*, 1484–1491.
(54) Huang, C. N.; Chen, S. Y.; Shen, P. *J. Phys. Chem. C* **2007**, *111*, 3322–3327.
(55) Mullin, J. W. *Crystallization*, 3rd ed.; Butterworth-Heinemann: Woburn, MA, 1997.
(56) Wulff, G.; Zeitschrift, F. *Beitr. Krystallogr. Mineral.* **1901**, *34*, 449.
(57) Si, R.; Zhang, Y. W.; You, L. P.; Yan, C. H. *Angew. Chem.* **2005**, *117*, 3320–3324.
(58) Pileni, M. P. *J. Phys. Chem. C* **2007**, *111*, 9019–9038.
(59) Wang, W.; Ao, L. *Cryst. Growth Des.* **2008**, *8*, 358–362.
(60) He, T.; Chen, D.; Jiao, X.; Wang, Y.; Duan, Y. *Chem. Mater.* **2005**, *17*, 4023–4030.
(61) Unveren, E.; Kemnitz, E.; Hutton, S.; Lippitz, A.; Unger, W. E. S. *Surf. Interface Anal.* **2004**, *36*, 92–95.

JP900226M

General Two-Phase Routes to Synthesize Colloidal Metal Oxide Nanocrystals: Simple Synthesis and Their Ordered Self-Assembly Structures

Thanh-Dinh Nguyen and Trong-On Do*

Department of Chemical Engineering, Laval University, Quebec G1K 7P4 Canada

To whom correspondence should be addressed. E-mail: Trong-On.Do@gch.ulaval.ca

SUBMITTED TO *J. Phys. Chem. C* – Jan. 2009

REVISED MANUSCRIPT: APRIL 2009

SUPPORTING INFORMATION

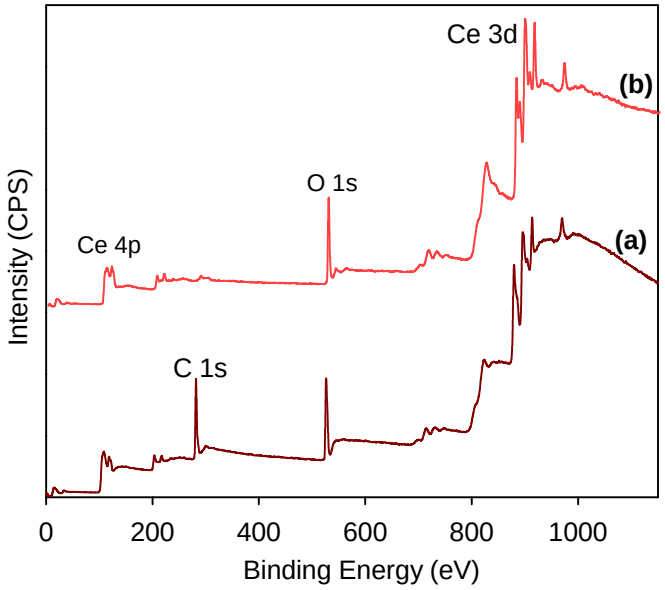

S-Figure 1. Survey XPS spectra of the CeO_2 nanocubic sample before (a) and after (b) calcination.

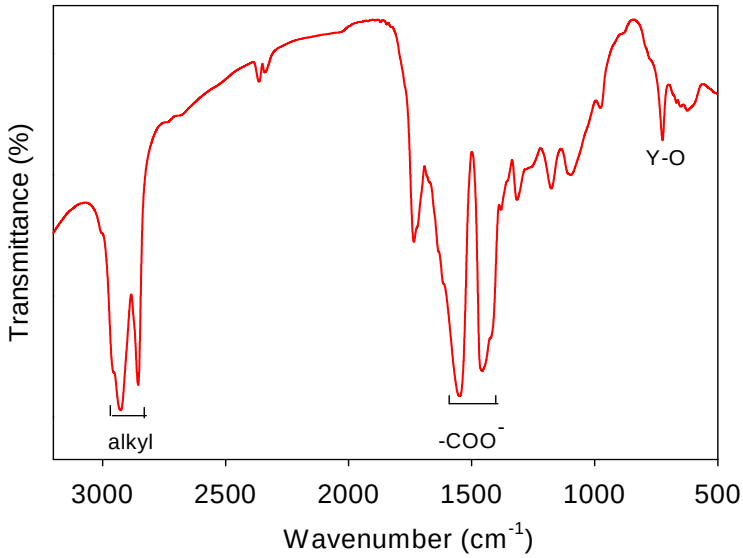

S-Figure 2. FTIR spectrum of Y-oleate complexes.

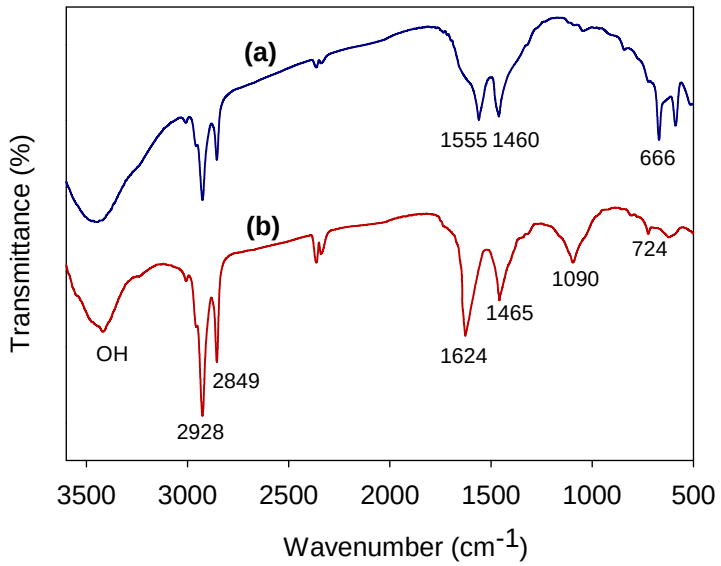

S-Figure 3. FTIR spectra of alkyl-capped metal oxide NCs: (a) OM-capped Y_2O_3 nanorods (sample 7) and (b) OA-capped Co_3O_4 nanospheres (sample 10).

The FTIR spectra of OM-capped Y_2O_3 and OA-capped Co_3O_4 NCs exhibit sharp peaks at 2828-2949 cm^{-1} attributed to the C-H stretching mode of methyl and methylene groups of the alkyl chains (S-Figure 7). The spectrum for OM-capped Y_2O_3 NCs shows the characteristic amide II band (1465-1624 cm^{-1}) resulting from the combination of N-H bending and N-C stretching of $–NH_2$ group of oleylamine.[16] For the OA-capped Co_3O_4 NCs, the broad IR bands at 1555 cm^{-1} and 1460 cm^{-1} attributed to the antisymmetric $\nu(COO^-)$ and the symmetric $\nu(COO^-)$ stretches of oleic acid.[23] The absorption bands at about 500-750 cm^{-1} correspond to vibrations of metal oxides. Furthermore, a broad band at 3250-3500 cm^{-1} is assigned to O-H vibrations of adsorbed water on the surface. This clearly indicates oleylamine or oleic acid molecules capped on the nanocrystal surface.

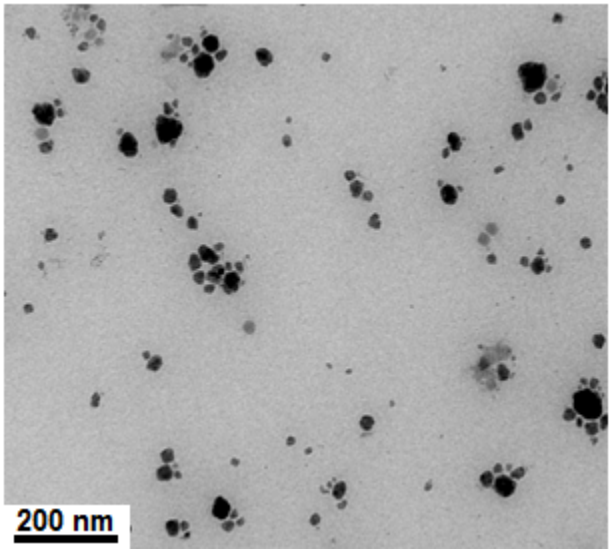

S-Figure 4. TEM image of as-made Y_2O_3 nanocrystals synthesized using $Y(ac)_3$ precursors following Scheme 1B.

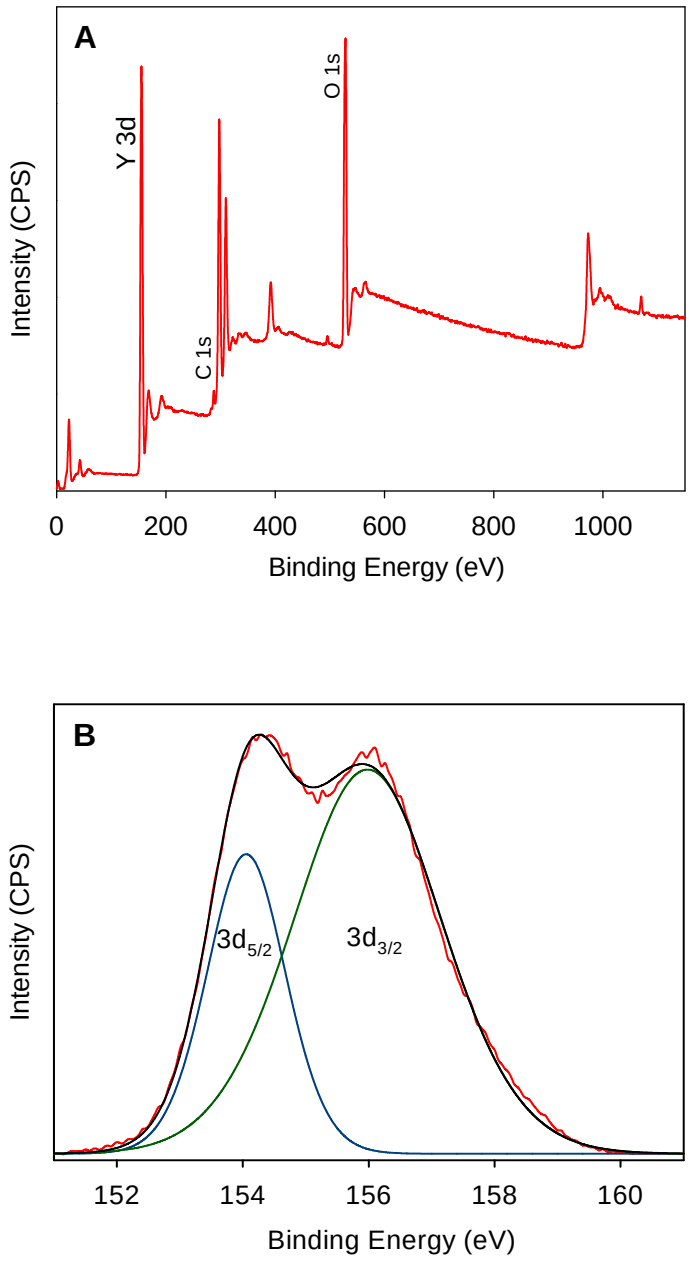

S-Figure 5. Survey XPS spectrum (A) and Y 3d XPS spectrum (B) of the calcined Y_2O_3 nanorods (sample 7).

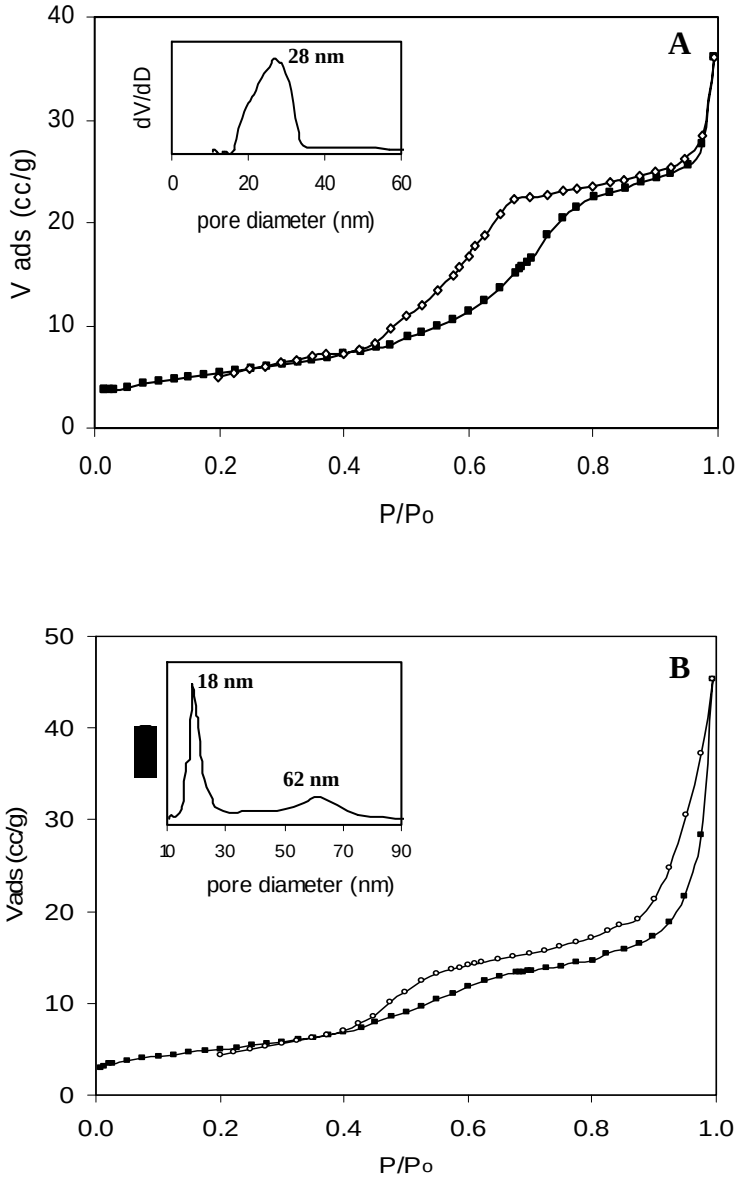

S-Figure 6. N_2 adsorption-desorption isotherms and corresponding pore size distribution curves (inset) for the calcined rare earth oxide NC samples: (A) Er_2O_3 (sample 4) and (B) Gd_2O_3 (sample 5).

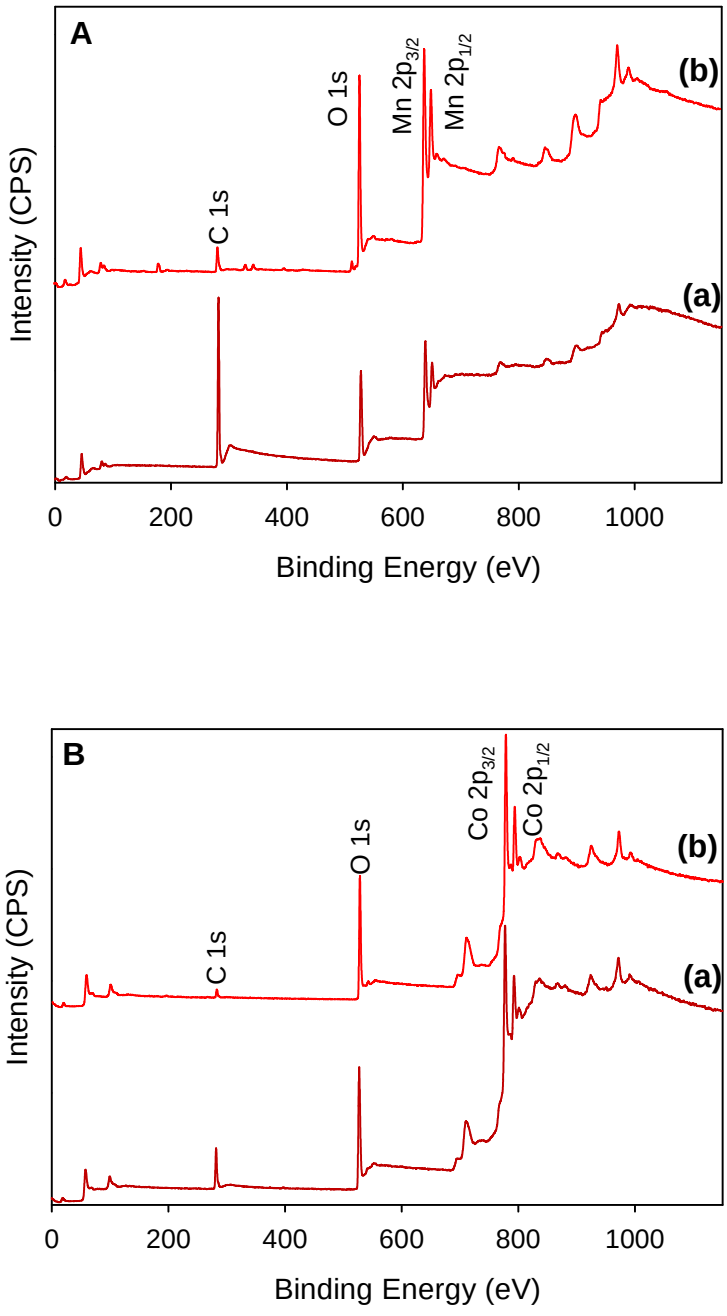

S-Figure 7. Survey XPS spectra in the wide energy range of the transition-metal oxide NC samples before and after calcination: (A) as-made (a) and calcined (b) hexagonal Mn_3O_4 nanocrystals; (B) as-made (a) and calcined (b) Co_3O_4 nanospheres.

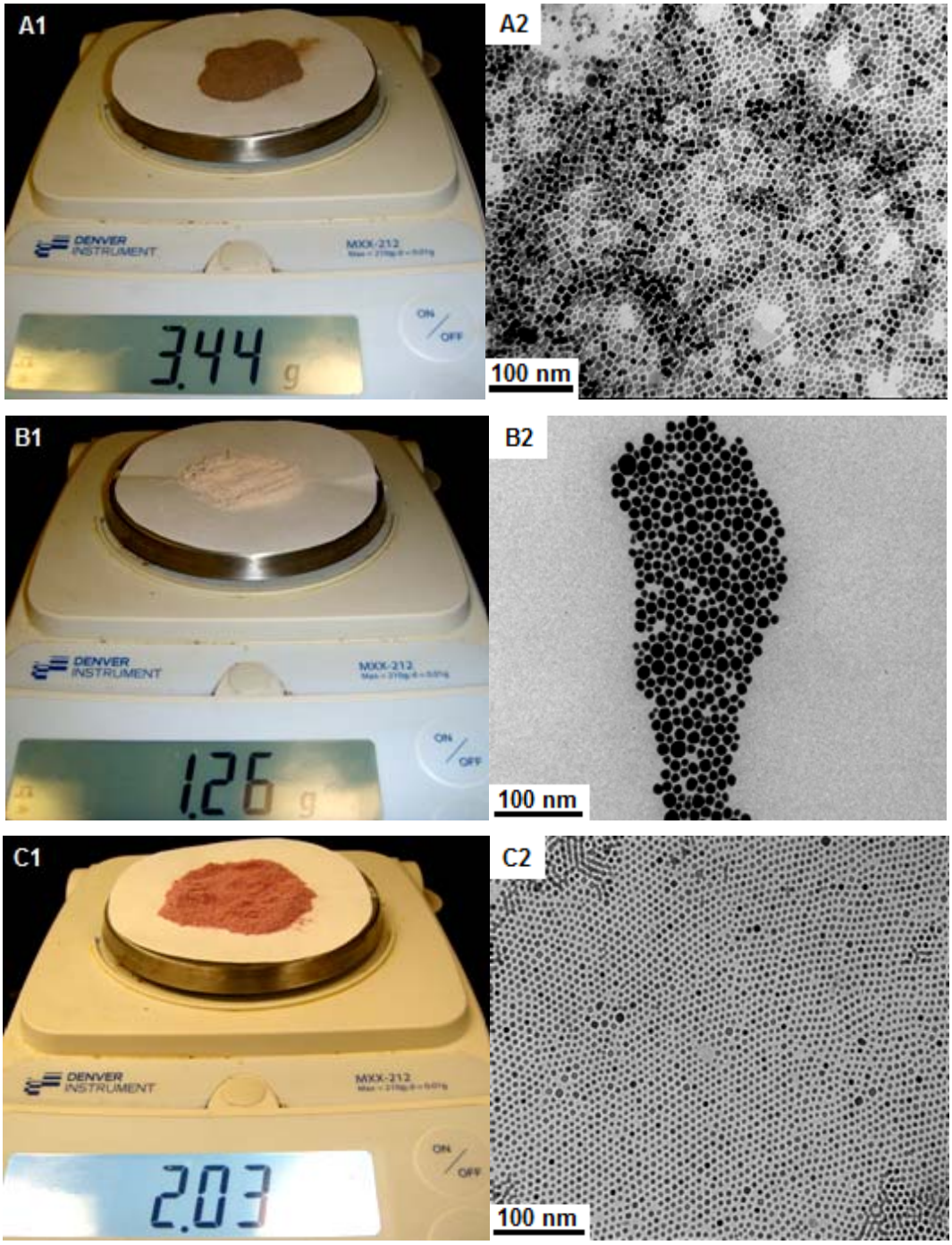

S-Figure 8. The color photographes and corresponding TEM images of the alkyl chain-capped metal oxide nanocrystals synthesized the muti-gram-scale products when the reaction size for the synthesis was increased by a factor of 12.5:

- (A_1) 3.4 g and (A_2) 6-8 nm size of OA-capped CeO_2 nanocubes;
- (B_1) 1.2 g and (B_2) 10-20 nm size of OM-capped Er_2O_3 nanospheres;
- (C_1) 2.0 g and (C_2) 5-7 nm size of OA-capped Co_3O_4 nanospheres.

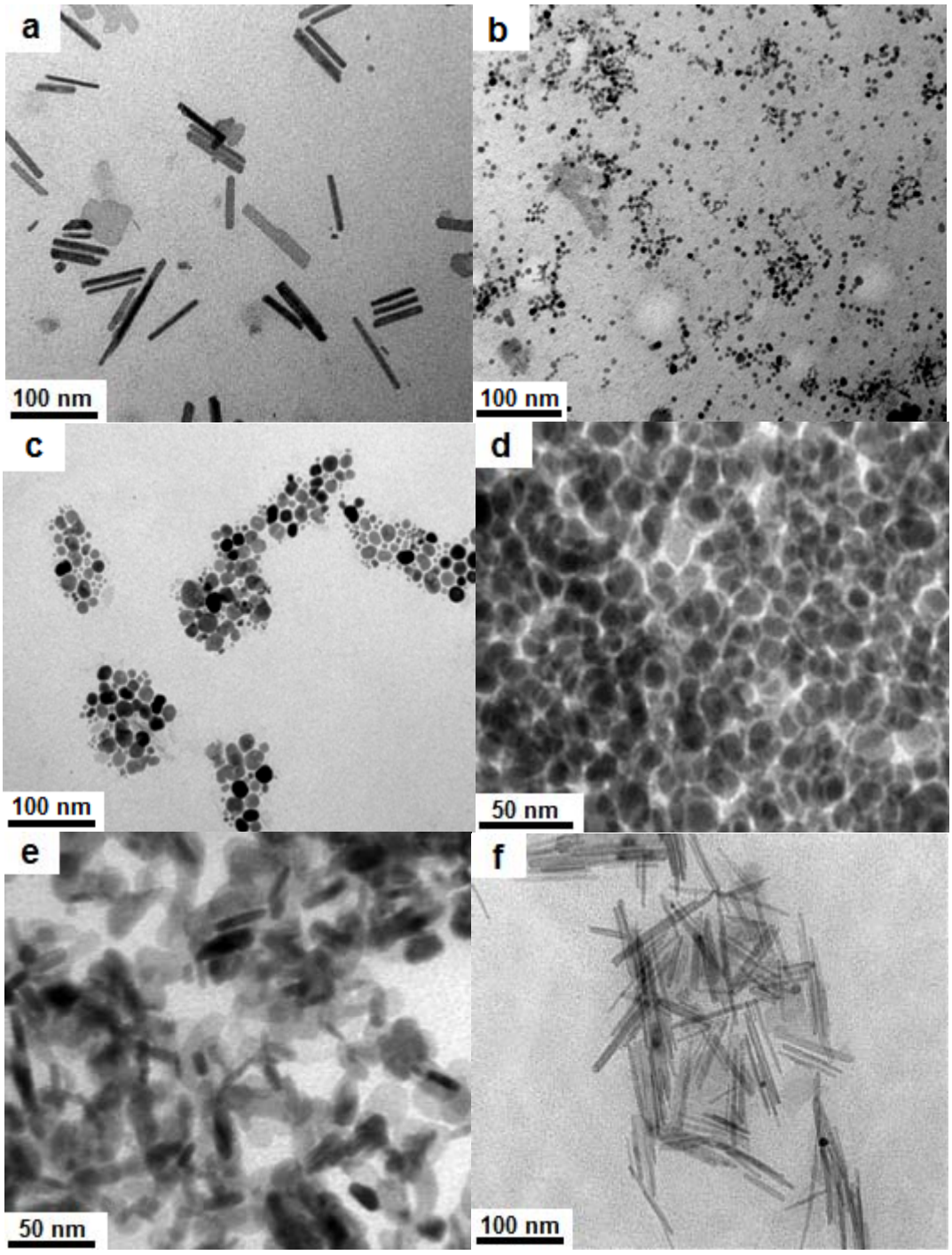
a
100 nm
b
100 nm
c
100 nm
d
50 nm
e
50 nm
f
100 nm

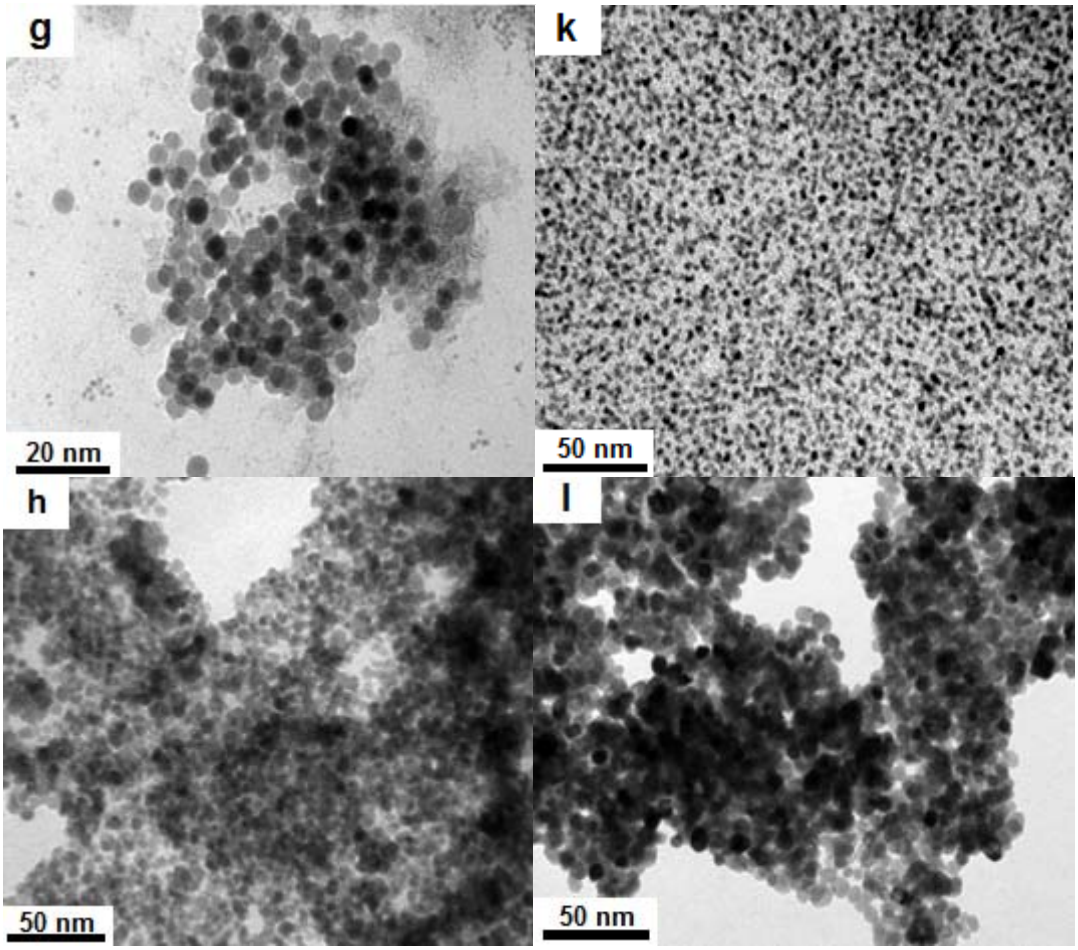

S-Figure 9. TEM images of the as-synthesized metal oxide nanocrystals after calcination in the air at 550^{o}C for 2 h: (a) Sm_2O_3 (calcined sample 1), (b) CeO_2 (calcined sample 2), (c) Er_2O_3 (calcined sample 4), (d) Gd_2O_3 (calcined sample 5), (e) La_2O_3 (calcined sample 6), (f) Y_2O_3 (calcined sample 7), (g) Mn_3O_4 (calcined sample 8), (k) Cr_2O_3 (calcined sample 9), (h) Co_3O_4 (calcined sample 10), and (l) NiO (calcined sample 13).